Article

Development of Global Snow Cover—Trends from 23 Years of Global SnowPack

Sebastian Roessler *[ID] and Andreas Jürgen Dietz [ID]

German Remote Sensing Data Center (DFD), German Aerospace Center (DLR), 82234 Wessling, Germany
* Correspondence: sebastian.roessler@dlr.de

Abstract: Globally, the seasonal snow cover is the areal largest, the most short-lived and the most variable part of the cryosphere. Remote sensing proved to be a reliable tool to investigate their short-term variations worldwide. The medium-resolution sensor MODIS sensor has been delivering daily snow products since the year 2000. Remaining data gaps due to cloud coverage or polar night are interpolated using the DLR's Global SnowPack (GSP) processor which produces daily global cloud-free snow cover. With the conclusion of the hydrological year 2022 in the northern hemisphere, the snow cover dynamics of the last 23 hydrological years can now be examined. Trends in snow cover development over different time periods (months, seasons, snow seasons) were examined using the Mann–Kendall test and the Theil–Sen slope. This took place as both pixel based and being averaged over selected hydrological catchment areas. The 23-year time series proved to be sufficient to identify significant developments for large areas. Globally, an average decrease in snow cover duration of -0.44 days/year was recorded for the full hydrological year, even if slight increases in individual months such as November were also found. Likewise, a large proportion of significant trends could also be determined globally at the catchment area level for individual periods. Most drastic developments occurred in March, with an average decrease in snow cover duration by -0.16 days/year. In the catchment area of the river Neman, which drains into the Baltic Sea, there is even a decrease of -0.82 days/year.

Keywords: snow cover; remote sensing; MODIS; Global SnowPack (GSP); trend analysis; Mann–Kendall (MK)

1. Introduction

Seasonal snow cover is globally the most noticeable part of the cryosphere. In terms of areal coverage, it is its largest component, but at the same time, the most short-lived and most variable. In the northern hemisphere, approximately 40–50% of the land surface is covered by snow during mid-winter [1,2]. Snow is an integral part of the climate system as it controls atmospheric processes due to its high albedo, low thermal conductivity and significant latent heat [3] and has therefore been classified by the World Meteorological Organization's (WMO) Global Climate Observing System (GCOS) as an Essential Climate Variable (ECV) [4]. Hydrologically, the seasonal snow cover is an important natural reservoir: it accumulates during the cold season, while meltwater is released again in warmer and drier periods and provides freshwater for over one billion people worldwide [5]. The smallest changes in timing and/or the amount of accumulated snow can have a drastic impact on runoff, phenology and water supply [6,7]. Since both small-scale and short-term changes in snow cover can have drastic effects for large regions, the GCOS places the following requirements on a global snow product: the snow-covered area should be recorded daily and the spatial resolution should be at least 1000 m (100 m in complex terrain). These requirements can only be met using remote sensing methods [8].

Both active and passive remote sensing systems offer opportunities for snow observation [9]. Passive microwave remote sensing has a long history in the analysis of the

snowpack since it is not influenced by clouds and can penetrate the snowpack. Thus, sensors such as the Scanning Multichannel Microwave Radiometer (SMMR) on Nimbus-7 have been used for this purpose since the early 1990s [10]. Although these sensors deliver daily information and also hydrologically relevant parameters such as the Snow Water Equivalent (*SWE*), their major drawback is their very coarse spatial resolution. Even newer sensors such as the Advanced Microwave Scanning Radiometer for EOS (AMSR-E) on Aqua have only a spatial resolution of 25 km [11]. Active microwave (Synthetic Aperture Radar; SAR) systems offer much better resolutions, but they are only capable of detecting melting (wet) snow [12]. High-resolution optical sensors such as the Landsat satellite family and Sentinel-2 offer a very good spatial resolution, which also allows analyses in the mountains [13], but they do not provide the desired temporal (daily) coverage. In order to meet the requirements specified by the GCOS (daily recording, at least 1000 m resolution), we therefore have to use medium-resolution optical remote sensing sensors such as the MODerate resolution Imaging Spectroradiometer (MODIS).

The MODIS snow products [14] have a long history in analysis of snow cover dynamics worldwide. The areas of application range from spatially limited areas such as the Himalayas [15] or the Andes [16,17] to global investigations such as albedo analysis [18]. Sensor fusion methods are also used to increase time series by combining MODIS data with AVHRR [19]. There are also methods for spatial downscaling of the information from MODIS with the help of high-resolution optical data from Sentinel-2 and/or Landsat-8 [20,21]—this is mainly carried out with regard to their applicability in mountains [22], where a spatial resolution of 100 m is required by GCOS.

Nevertheless, there is a disadvantage here too: optical systems can only deliver correct data in daylight and in a cloud-free atmosphere—which inevitably leads to data gaps. To solve this issue, various methods have been developed to fill these gaps [15,23]. One of these methods is the Global SnowPack (GSP) [24] product developed at the German Aerospace Center (Deutsches Zentrum für Luft- und Raumfahrt; DLR), whose time series, now covering 23 hydrological years, is examined in this study.

Large-scale analyses of the snow cover development have been carried out by [25] who found a decrease in Snow Cover Extent (SCE) of 1 million km^2 (or 4%) for the entire Northern Hemisphere compared to the long-term mean since 1966–2020. For the global mountain ranges, [22] found for 38 observed years (1982–2020) a mean SCE decrease of $-3.6\% \pm 2.7\%$, and a Snow Cover Duration (*SCD*) decrease of -15.1 days ± 11.6 days. Our study will focus on changes in the *SCD* and also on different time periods—since drastic changes in the *SCD* can occur on a small scale and are limited to a few months, such as an increase in the *SCD* during the boreal spring in the Sápmi region (North Fennoscandia) [26]. A shift in the *SCD* was found particularly in continental areas; [27] analyzed snow data in Canada from 185 stations and found an *SCD* decrease of -1.68 days/decade in the boreal autumn and an increase of $+0.28$ days/decade in the boreal spring.

The scope of this study is the global analysis of the snow cover data, now covering 23 hydrological years. Different periods of time are examined with proven methods of trend analysis [15,28–30]. This took place as both pixel based and aggregated to hydrological catchment areas [31–33]. The following three research questions should be answered:

1. Are 23 years sufficient to detect significant trends in snow cover development?
2. Is the comparatively small FAO data set with the aggregated major basin areas suitable to allow statements for hydrologically defined areas?
3. In which areas (pixel and basin based) are trends identified?

The novelty of our approach is that we use gap-free data from 119 MODIS tiles worldwide and for a period now spanning 23 years on a daily basis to make high-resolution global statements on snow development and at the same time extract them for selected hydrological units. In addition, the availability of the GSP data in near real-time enables very up-to-date processing. The analysis already includes the hydrological year 2022, which ended on 31 August 2022 in the northern hemisphere. The article is structured as follows: First, the data set and methods used are presented. Then, they are shown

according to the selected criteria for the major basin areas. Finally, the developments of the most conspicuous time periods (seasons) are shown in the Results section (each for the pixel-based and basin-based evaluation).

2. Materials and Methods

2.1. Snow Cover Extent

Information on global snow coverage is derived from the MODIS sensors onboard the satellites Terra (since 02/2000) and Aqua (since 07/2002). Based on the Normalized Difference Snow Index (*NDSI*) [34], the daily snow cover products MOD10A1 [35] (Terra) and MYD10A1 [36] (Aqua) are made available free of charge by the National Snow and Ice Data Center (NSIDC) [14]. The data set is available in the sinusoidal projection—a pseudo cylindrical equal-area map projection [37]. The globe is further subdivided into 36 horizontal and 18 vertical tiles, the snow product is only calculated for tiles where land areas exist. Figure 1 shows an example of a daily composite of the layer "*NDSI_snow_cover*".
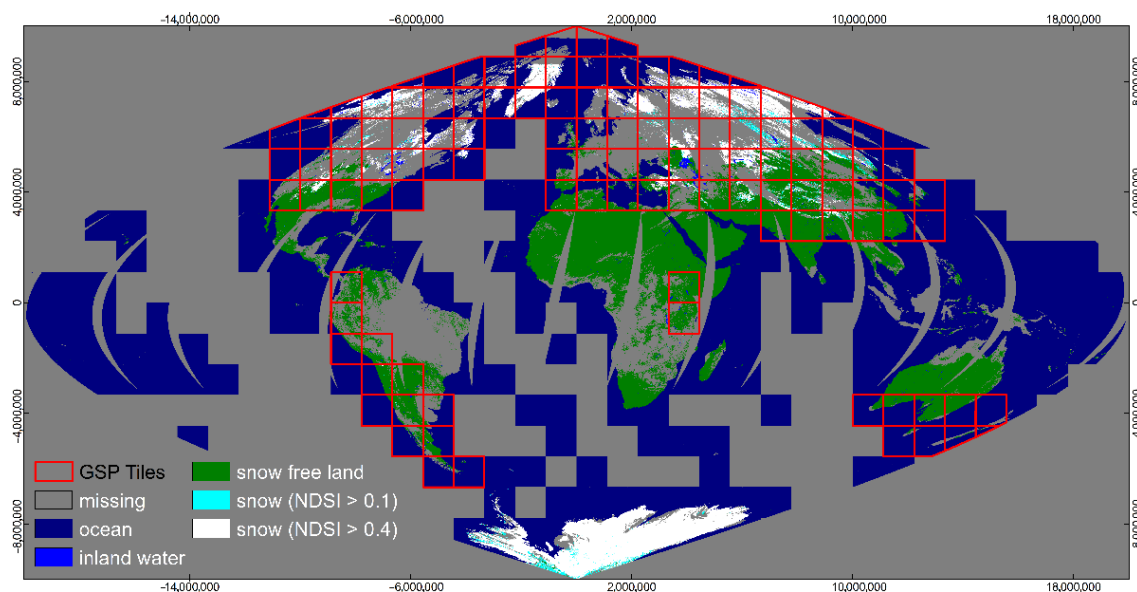
Figure 1. Global Mosaic of Terra Snow Product MOD10A1 from 12 March 2008. The 119 tiles used for GSP are framed in red (Antarctica is not included in this study).

The *NDSI* uses the spectral property of snow; it has a high reflectance in the visible spectrum (*VIS*), but has a low reflectance in the short-wave infrared (*SWIR*). The calculation is based on Equation (1) [38]:

$$NDSI = \frac{\rho_{VIS} - \rho_{SWIR}}{\rho_{VIS} + \rho_{SWIR}},\qquad(1)$$

where ρ_{VIS} is the reflectance in the green wavelength region (band 4 for MODIS: 545–565 nm), ρ_{SWIR} is the *SWIR* reflectance (band 6 for MODIS: 1.628–1.652 µm). The *NDSI* can take values between −1 and +1, and is related to fractional Snow Cover Area (*fSCA*) by the linear relationship $fSCA = 0.06 + 1.21 * NDSI$ [39]. Thus, a *NDSI* of 0.4 represents a *fSCA* of 54.4%. While the *NDSI* threshold of 0.4 is often used in the literature to create binary snow masks (because most of the area is snow-covered), an underestimation can occur especially in coniferous forests [40]. Therefore, the *NDSI* is combined with the Normalized Difference Vegetation Index (*NDVI*) to also assign low *NDSI* values (0.1–0.4) to a binary snow mask if the *NDVI* is high enough at the same time. The *NDSI* values in the "*NDSI_snow_cover*" layer are already quality checked and scaled from 0 to 100, where a value greater than or equal to 10 represents snow cover.

Figure 1 also shows the following: there are numerous data gaps in the daily product, whether due to lack of coverage (especially near the equator), cloud cover or the polar night. However, to establish the complete duration of snow cover, these gaps must be filled. Spatial and temporal approaches were developed for this [41]. The Cloud-Gap Filled (CGF) products of the NSIDC provides Terra (MOD10A1F) and Aqua (MYD10A1F) data that are filled with values from previous sources in a temporal approach [23]. Other approaches use spatial filling (by surrounding pixels), or a combination of both methods [42]. The GSP method is a multi-sensor, spatial and temporal gap-filling approach and runs in four consecutive steps [24]:

1. Daily combination: Merging the daily snow cover maps of Terra and Aqua (if both are available). Terra data are given preferential treatment, since channel 6, which is required for the *NDSI* calculation, does not work with Aqua and band 7 is used here instead.
2. Three-day interpolation: Gaps in the current day are filled with data from the following day, then with data from the previous day.
3. Topographic interpolation: If the cloud cover of the land pixels in each tile is below 30%, the absolute upper snow line (altitude level above which only snow occurs) and the absolute lower snow line (altitude level below which only snow-free pixels occur) are determined with a digital elevation model. Pixels with altitudes above the absolute upper snow line are classified as snow, and pixels with altitudes below the absolute lower snow line as snow-free.
4. Seasonal interpolation: In the last step, the remaining gaps are filled by a temporal interpolation over the previous days. The number of days to fill is stored in a separate array and is used for accuracy estimation.

The result is a gap-free global binary (either snow-covered or snow-free) snow cover map for each day of the hydrological year. From this, the duration of snow cover for different periods can now be calculated.

2.2. Snow Cover Duration

The *SCD* represents the number of days when each pixel is covered by snow during a certain period of time [43]. It is calculated based on Equation (2):

$$SCD_{period} = \frac{\sum_{i=0}^{n} S_i}{n},\tag{2}$$

where S_i are the snow-covered pixels and n is the amount of days in the observed *period* of time. A normalization to values between 0 and 1 was carried out in order to avoid distortions caused by leap years. The periods of time considered in this study are described in Table 1.

The hydrological year was chosen for the division of the snow seasons. We define its start with the beginning of the meteorological autumn, which is in the northern hemisphere (*NH*) on September 1st, and in the southern hemisphere (*SH*) on March 1st. The name for the hydrological year is always the year in which it ends. The hydrological year 2001 begins in the northern hemisphere on 1 September 2000 and ends on 31 August 2001, in the southern hemisphere it begins on 1 March 2000 and ends on 28 February 2001. Snow seasons are further divided into an early and late season, which should represent snow accumulation and melting of snow [44]. The time of the separation is the maximum snow cover, which corresponds to mid-winter (i.e., 15 January in the northern hemisphere, 15 July in the southern hemisphere) [45]. The sum of "early" and "late" snow cover duration then forms the snow cover duration over the entire (hydrological) year and is referred to as "full". Figure 2 shows the global mean annual snow cover duration ($\overline{SCD_{full}}$) which was used to select the major catchment areas.

Table 1. Selected periods in this study. In addition to the months, there are meteorological seasons and snow seasons (based on hydrological years).

| Period of Time		Start	End	Days
01		1 January	31 January	31
02		1 February	28/29 February [1]	28/29 [1]
03		1 March	31 March	31
04		1 April	30 April	30
05		1 May	31 May	31
06		1 June	30 June	30
07		1 July	31 July	31
08		1 August	31 August	31
09		1 September	30 September	30
10		1 October	31 October	31
11		1 November	30 November	30
12		1 December	31 December	31
SON		1 September	30 November	91
DJF		1 December	28/29 February [1]	90/91 [1]
MAM		1 March	31 May	92
JJA		1 June	31 August	92
Early snow season	NH	1 September	14 January	136
	SH	1 March	14 July	
Late snow season	NH	15 January	31 August	229/230 [1]
	SH	15 July	28/29 February [1]	
Full snow season	NH	1 September	31 August	365/366 [1]
	SH	1 March	28/29 February [1]	

[1] in leap years.
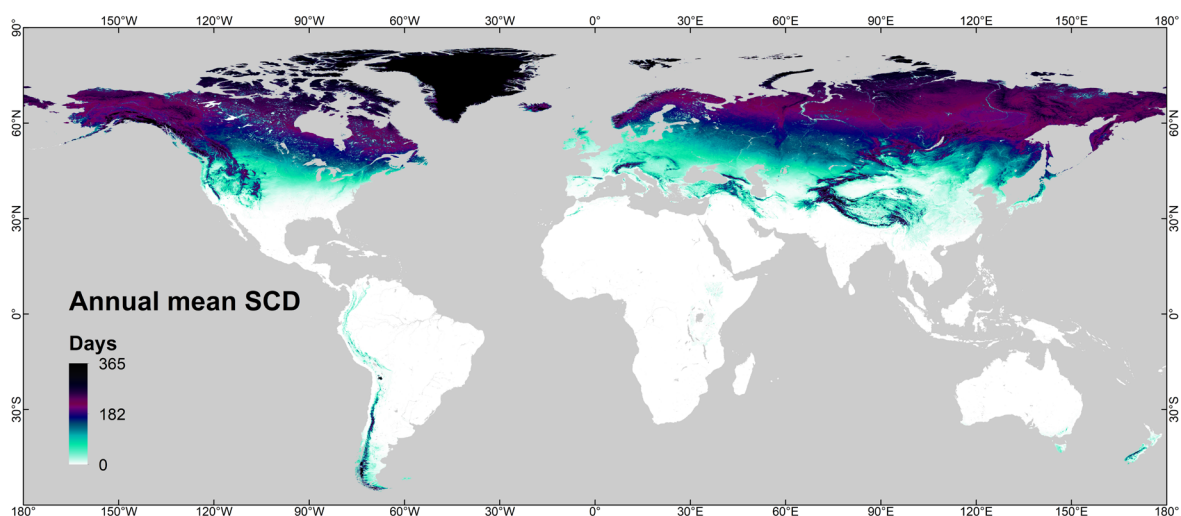
Figure 2. Annual mean snow cover duration ($\overline{SCD_{full}}$) derived from 23 hydrological years (2000–2022).

### 2.3. Selection of Major Basins

In addition to the pixel-based analysis of the development of the snow cover duration, the trend test was also applied to hydrologically delimited areas. For this, we used watershed boundary data that are provided by the Food and Agriculture Organization (FAO) [46]. Here, catchment areas with similar properties are merged into major basin areas, which leads to a manageable number of 231 basins worldwide. The selection of the major basin areas affected by snow was guided by $\overline{SCD_{full}}$ (Figure 2). For each basin, $\overline{SCD_{full}}$ was clipped using the shapefile and the Snow Cover Fraction (*SCF*) [47,48] was derived using the mean value of all valid pixels. To obtain full days, this value was multiplied by 365.25 days. An empirically determined threshold of >50 days was set to obtain

snow-affected catchment areas. Figure 3 shows the selected 57 major basins that were included in the analysis.
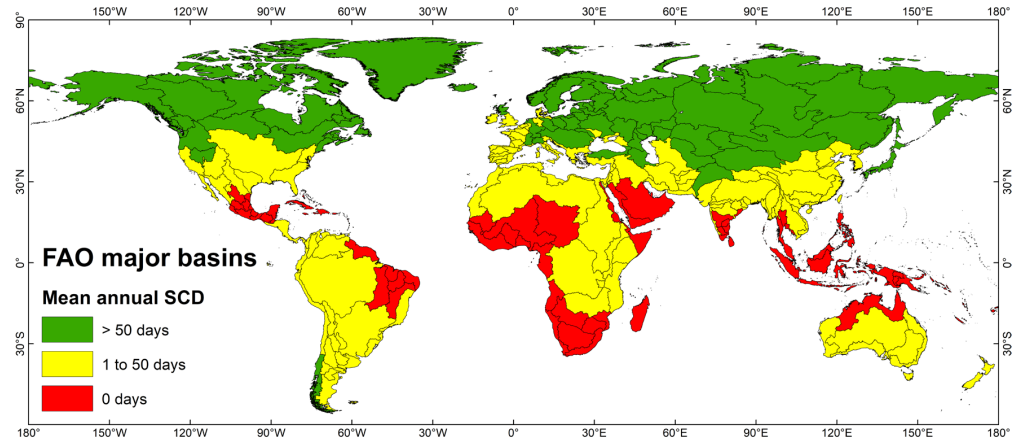
Figure 3. Overview of the catchment areas that are included in the analysis (green), that have only sparse snow cover (yellow) and that have no snow cover at all (red) (basins obtained from [46]).

Figure 4 shows the selected catchment areas sorted according to their area extent and their average snow coverage. The largest catchment areas are the Siberian West Coast, the Northwest Territories and the Ob River. The greatest snow coverage is achieved for the islands of the Arctic Ocean (since Greenland is part of them).
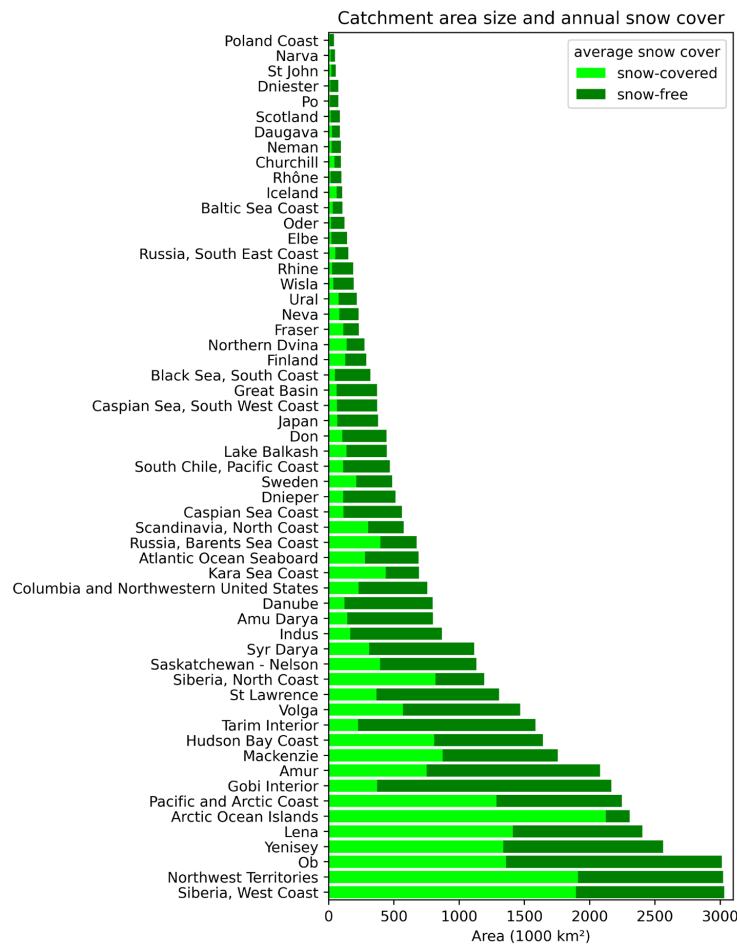
Figure 4. Overview of the area extent of the selected basins and their mean snow cover (basins obtained from [46]).
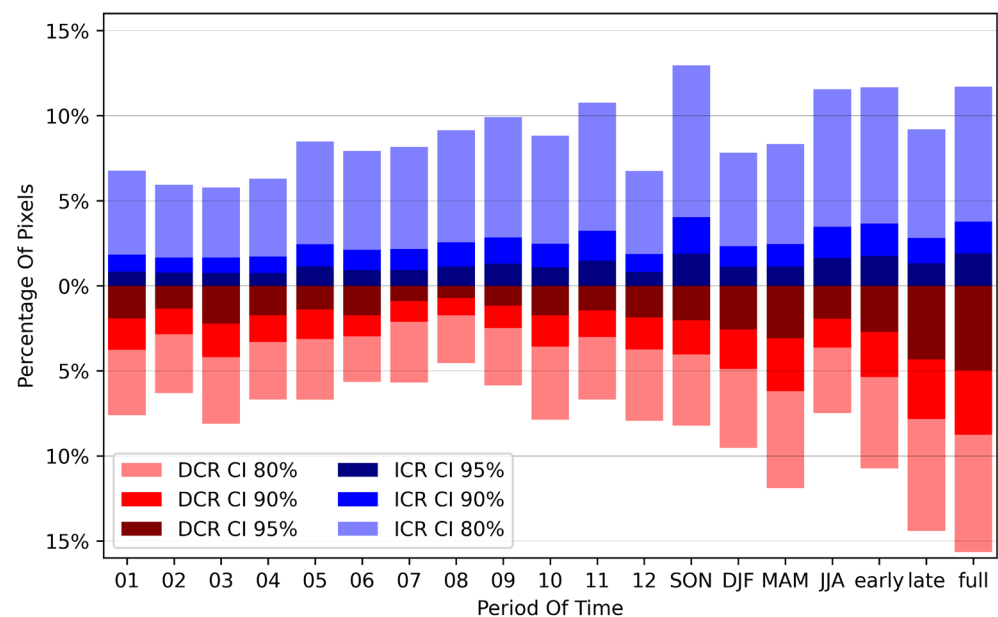
2.4. Trend Analysis

The Mann–Kendall (MK) test [49,50] was performed to analyze the statistical significance of the trends of *SCD*. For each of the 19 periods of time listed in Table 1, the entire time series of 23 years was examined. In the MK test, a null hypothesis (H_0), which states that there is no monotonic trend, was tested against three possible alternatives: (i) there is an increasing monotonic trend, (ii) there is a decreasing monotonic trend, or (iii) there is neither a descending, nor an ascending monotonic trend. The null hypothesis is rejected if the *p*-value is less than the predefined significance level. We used significance levels of 0.05, 0.1 and 0.2. Since no autocorrelation was found in the data sets, the original test was used. The magnitude of the trend was determined by the Theil–Sen slope [51], which, in contrast to linear regression, is more robust against outliers. The trend analysis was performed in Python 3.9, for the combination of Mann–Kendall Test and Theil–Sen Slope the package *pyMannKendall* [52] was used. For the pixel-based analysis, the MK test was performed for all valid land pixels (i.e., ocean and inland water bodies are omitted). For the basin-based analysis, the mean *SCD* of the entire catchment area was used for the analysis. Details on the calculation can be found in Appendix A.

3. Results

Due to the large number of seasons examined, only a small selection can be shown in this section. Therefore, it is restricted to the most relevant periods with the largest number of significant developments (pixel and basin based). Additionally, the histograms of all Theil–Sen slopes and the mean slopes for each confidence interval are summarized in Appendix B.

3.1. Pixel-Based Analysis

The pixel-based trend analysis was performed for all 119 tiles for the 19 seasons mentioned (a total of 2261 analyses). In order to determine which periods have a particularly large number of significant developments, the percentage of pixels that fall within the 95%, 90% and 80% confidence interval (CI) was determined both for increasing (ICR) and decreasing (DCR) developments of *SCD*. The result is shown in Figure 5.


Figure 5. Overview of the results of the pixel-based trend analyses. The number of pixels (percentage of all 371 Mio. Pixels) are shown that have a significant trend in the confidence intervals (CI) 80%, 90% and 95%. The decreasing (DCR) developments of the *SCD* are shown in red, the increasing (ICR) developments are shown in blue.

As can be seen from Figure 5, there are no distinct seasons that are showing extreme developments, but in general, the monthly trends have less significant areas than the meteorological seasons. In turn, these have less significant developments than the snow-seasonal developments. This applies equally to all confidence levels. However, since the associated Theil–Sen slopes show very pronounced developments in some seasons, we will show the most interesting ones:

3.1.1. Pixel-Based *SCD* Trend for March (03)

In March, the *SCD* development is significant for 12% of the area in the 80% confidence level (3% in the 95% confidence level). Figure 6 shows the areas where significant developments are taking place and also indicates the magnitude of the developments.
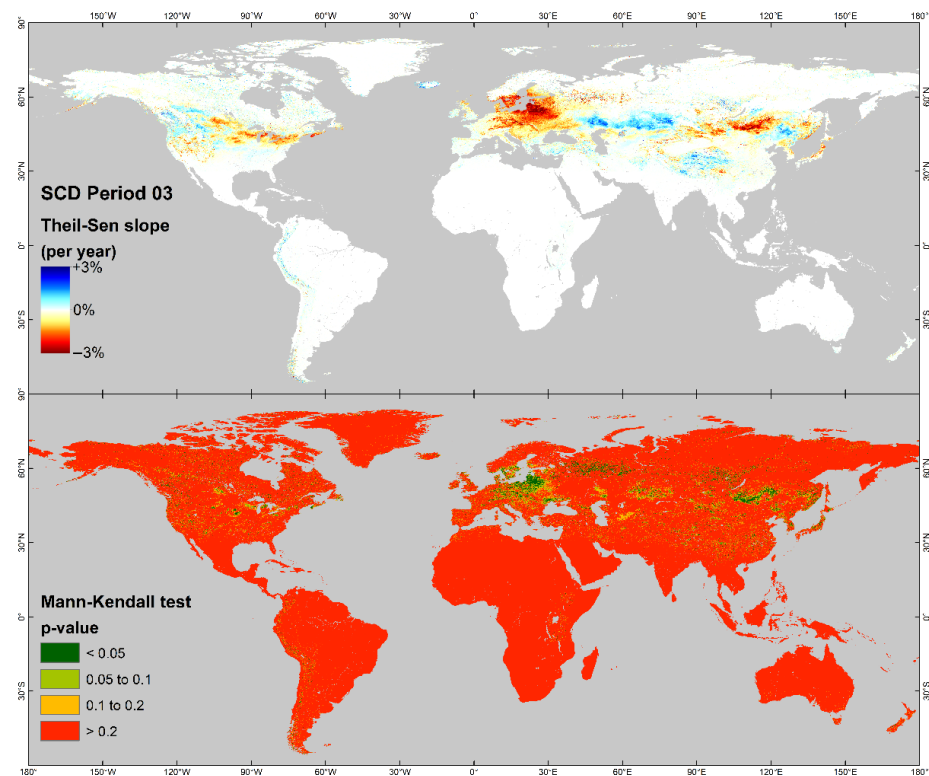
Figure 6. Pixel-based development of *SCD* in March. The Theil–Sen slope is shown above and the associated *p*-values are shown below.

The decrease in the *SCD* in the Baltic Sea region is particularly striking, and there are also significant decreases in the Siberian mountains, as well as in North America (from Lake Winnipeg to the Great Lakes). However, the large areas of increase in *SCD* in Central Asia are not significant.

3.1.2. Pixel-Based *SCD* Trend for April (04)

In April, the number of significant pixels is not extraordinarily high (11% at 80% confidence level, 3% at 95% confidence level). Figure 7 shows why this month is special.

In North America, particularly in southern Canada, large areas show an increase in *SCD*, although only few areas are significant. The situation is different in Eurasia. A mostly significant decrease in *SCD* can be observed over a broad strip stretching from the Baltic Sea over Lake Baikal to Japan.
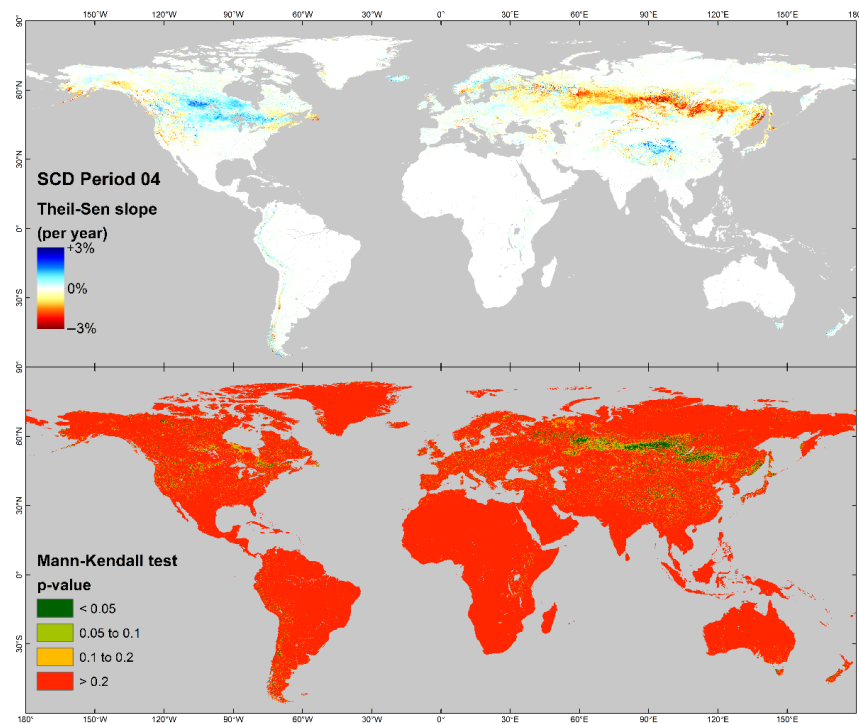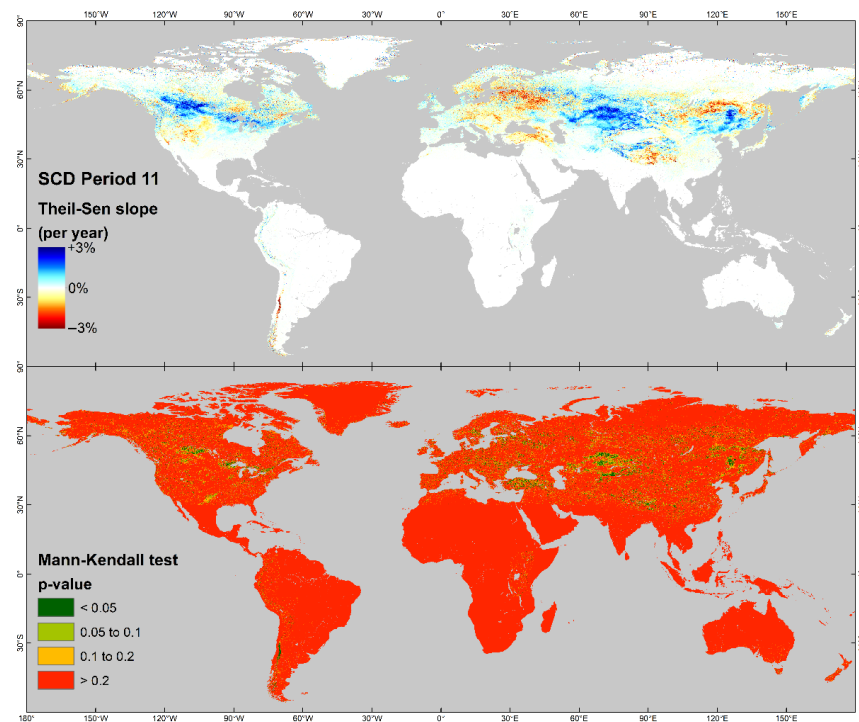
Figure 7. Pixel-based development of *SCD* in April. The Theil–Sen slope is shown above and the associated *p*-values are shown below.

3.1.3. Pixel-Based *SCD* Trend for November (11)

With 22% significant pixels (in the 80% confidence level), November shows the highest value in the monthly analysis (3% in the 95% confidence level). Figure 8 shows that this month is particularly marked by an increase in the *SCD*.
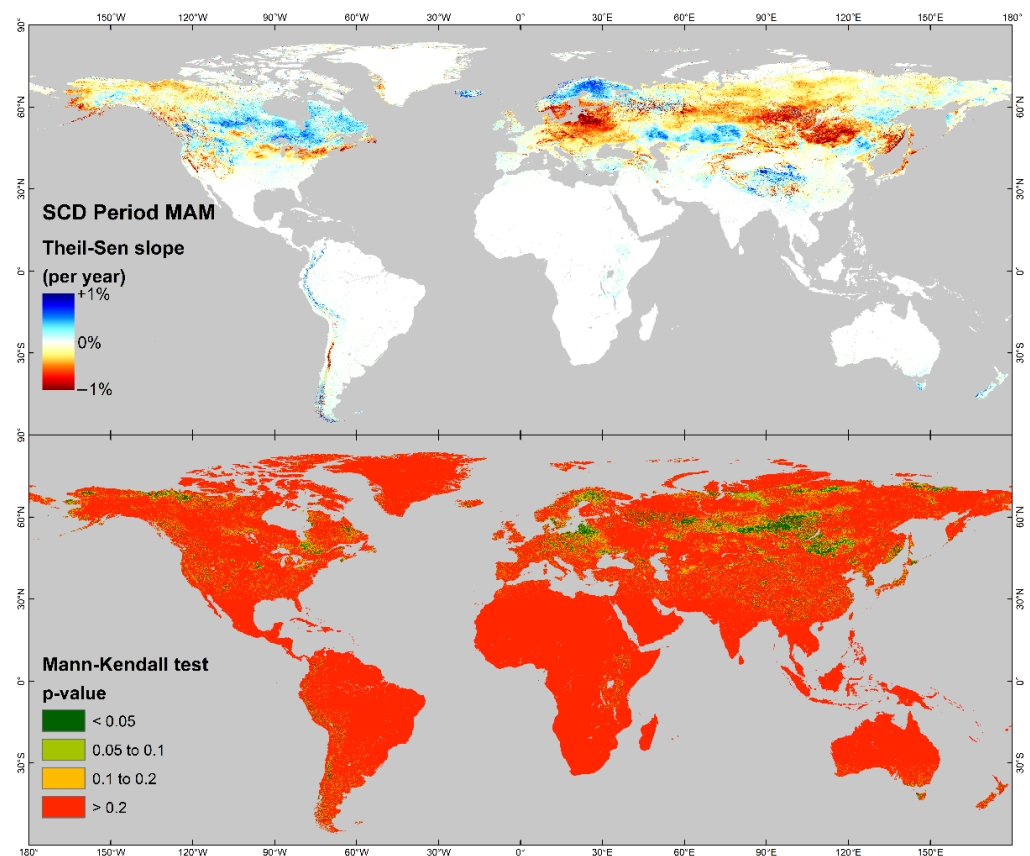

Figure 8. Pixel-based development of *SCD* in November. The Theil–Sen slope is shown above and the associated *p*-values are shown below.

In November, a (mostly significant) increase in *SCD* is observed in much of Canada. A similarly strong increase can be seen in Central Asia and in China in the area of Manchuria.

3.1.4. Pixel-Based *SCD* Trend for Boreal Spring (MAM)

In the boreal spring (March–May), almost 18% of the pixels achieve significant developments of *SCD* (80% confidence level; 4.3% in the 95% confidence level). Figure 9 shows the development in this meteorological season.

While the prevailing increase in *SCD* in North America is not significant, the sometimes drastic *SCD* decreases in Eurasia are mostly significant. A significant increase can also be observed in northern Europe in the area of Sápmi.
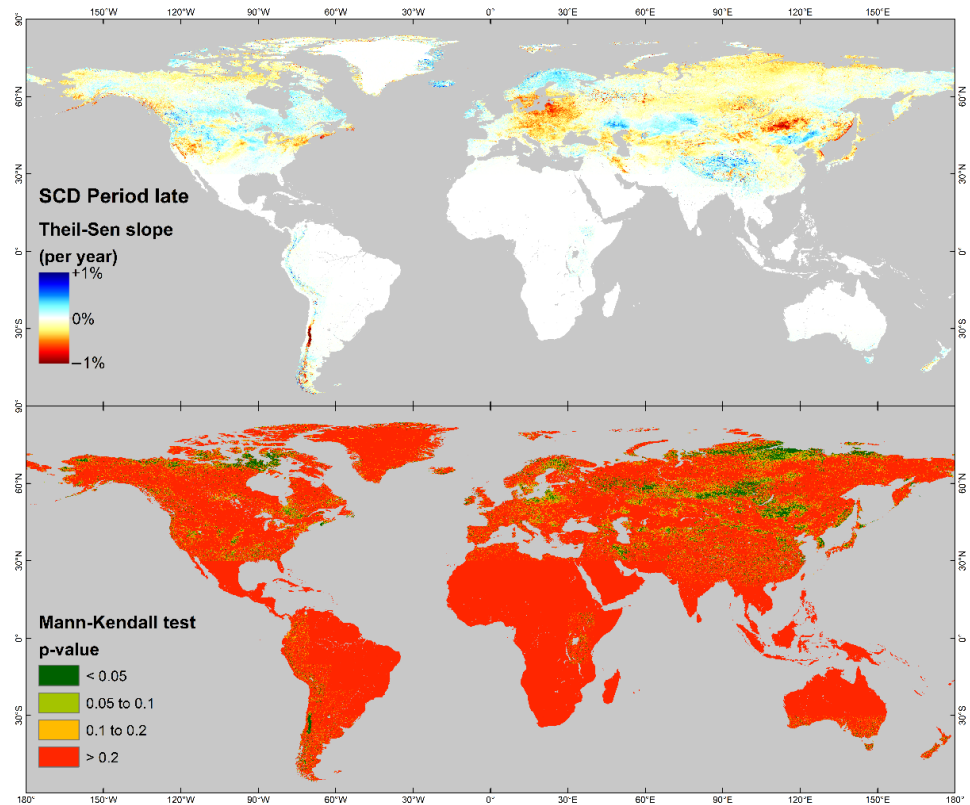

Figure 9. Pixel-based development of *SCD* in the meteorological season MAM. The Theil–Sen slope is shown above and the associated *p*-values are shown below.

3.1.5. Pixel-Based *SCD* Trend for Late Snow Season

In the late snow season, 21% of the pixels show significant development at the 80% confidence level (6% at the 95% confidence level). Figure 10 shows the *SCD* developments.

This season, especially in the far north of Canada and Russia, there is a significant decrease in snow cover duration. The significant decrease in the Baltic Sea region, which was already determined for March, is also reflected here.

Figure 10. Pixel-based development of *SCD* in the late snow season. The Theil–Sen slope is shown above and the associated *p*-values are shown below.

3.2. Basin-Based Analysis

The *SCD* development averaged over all pixels of the 57 selected FAO main basin areas show in general similar results. However, in contrast to the pixel-based trend analysis, three periods of time are emerging in which a larger number of basins shows significant developments of *SCD* (Figure 11).
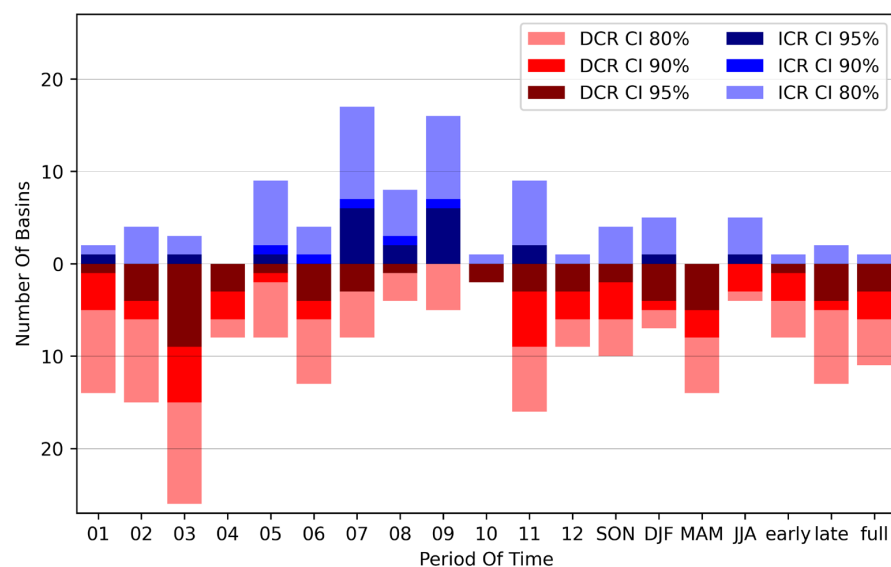
Figure 11. Overview of the results of the basin-based trend analyzes. It is shown how many major basins have a significant trend in the confidence intervals (CI) 80%, 90% and 95%. The decreasing (DCR) developments of the *SCD* are shown in red, the increasing (ICR) developments are shown in blue.

The two months of March and November, as well as the late snow season, stand out here and will be examined in more detail. Figure 12 summarizes the development of all 57 catchment areas for the 19 seasons.
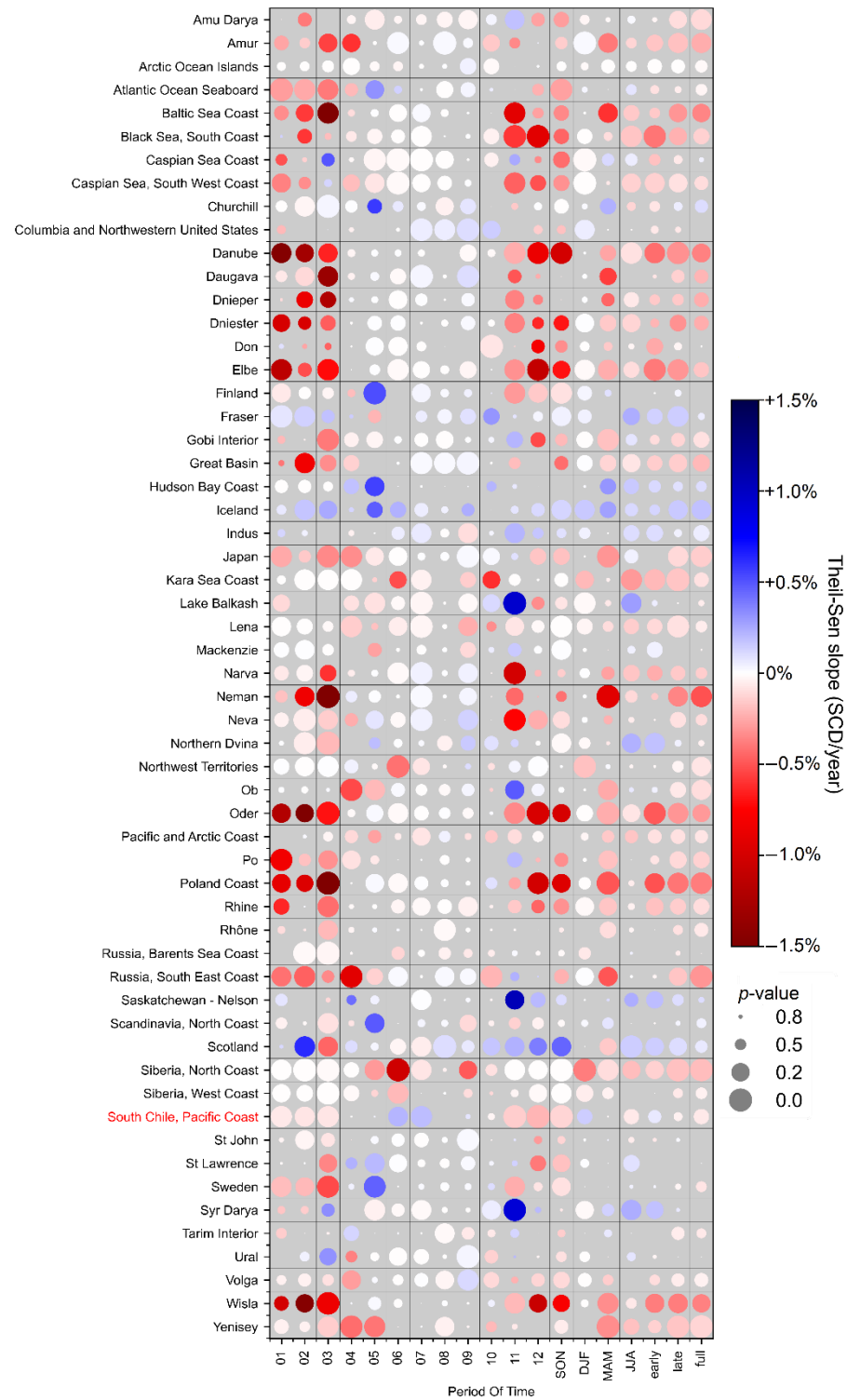
Figure 12. Summary of the trend analysis for the 57 studied major basin areas for the 19 periods of time. The color shows the magnitude of the *SCD* development (changes in duration percentage), the circle size indicates the significance (the larger, the closer the *p*-value is to 0). The only basin on the southern hemisphere is shown in red on the y-axis.

3.2.1. Basin-Based *SCD* Trend for March

As already seen from the pixel-based analysis, the region surrounding the Baltic Sea in particular is a hotspot of the *SCD* decrease in March. This is also reflected in the analysis of the major basin areas for this month. A total of 18% of the examined basins show a significant development of the *SCD* in the 95% confidence level (almost 50% do so in the 80% confidence level). Figure 13 shows the magnitudes and significance for this month.
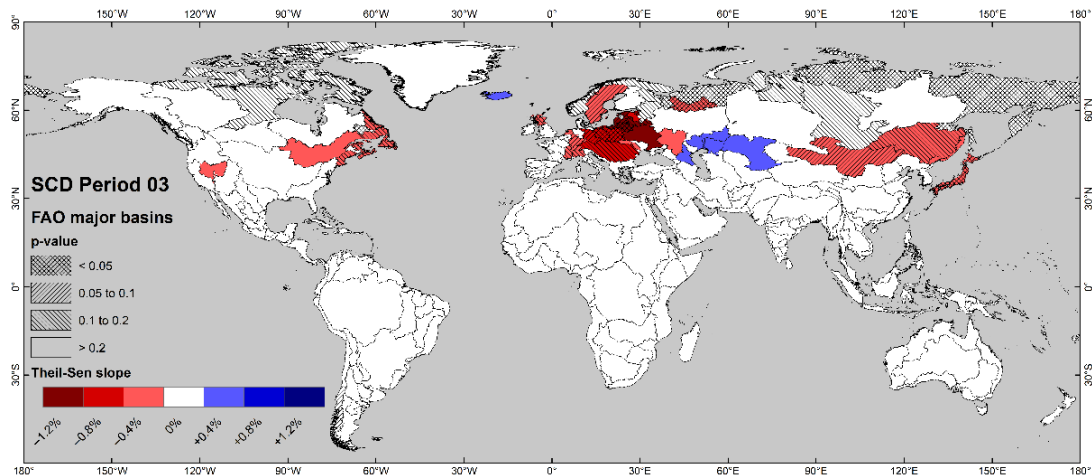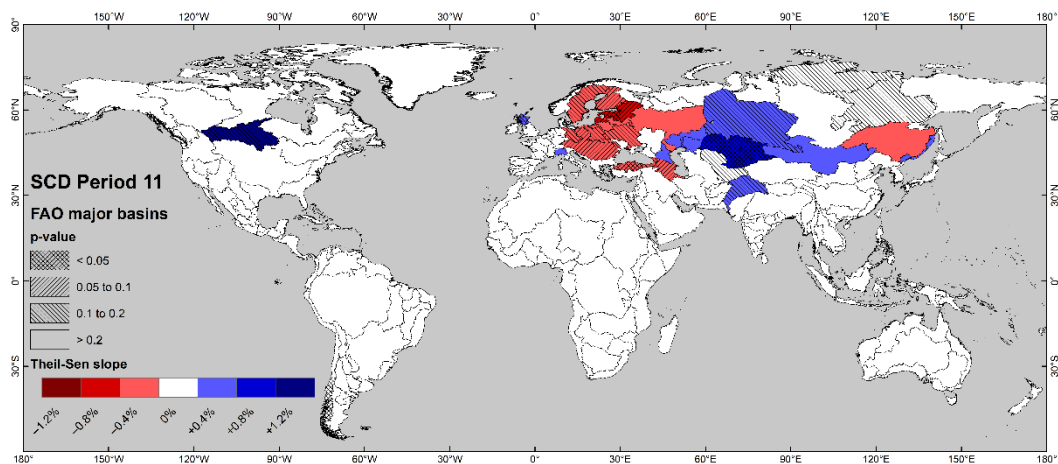

Figure 13. Basin-based development of the *SCD* in March. The Theil–Sen slope is color coded and the corresponding *p*-values are hatched over it.

As mentioned, it is above all the catchment areas that drain into the Baltic Sea that the strongest trends are shown here. For Wisla, it is -0.26 days/year for this month; on the Poland coast, it is -0.47 days/year; and on the river Oder, it is -0.22 days/year. However, the catchment area of the Neman River, which flows through Belarus, Lithuania and the Russian enclave of Kaliningrad, has the strongest trend at -0.85 days/year. Positive trends can be seen in Iceland and some basins in Central Asia; however, their development is not significant.

3.2.2. Basin-Based *SCD* Trend for November

The month of November shows the second strongest trends with a significant development of 40% of all basin areas (in the 80% confidence level); however, only five catchment areas (9%) are significant in the 95% confidence level. Figure 14 shows the developments for the month of November.
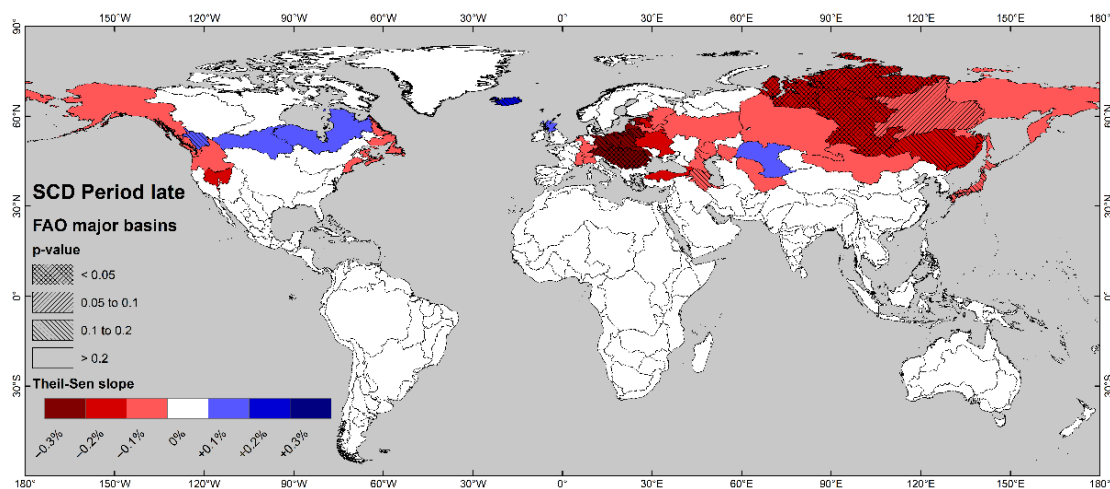

Figure 14. Basin-based development of the *SCD* in November. The Theil–Sen slope is color coded and the corresponding *p*-values are hatched over it.

The catchment areas of the Narva (the border river between Estonia and Russia) show significant negative developments this month with −0.3 days/year and the southern coast of the Black Sea with −0.18 days/year. However, the trends of two catchments in Central Asia are more striking: the Lake Balkash catchment at +0.29 days/year and the Syr Darya catchment at +0.27 days/year. The maximum significant *SCD* increase (within the 80% confidence level) shows the catchment area of the Nelson River in Canada/Unite States with +0.31 days/year.

3.2.3. Basin-Based *SCD* Trend for Late Snow Season

In terms of snow seasons, the late season *SCD* shows the most significant developments with 26% of all basins in the 80% confidence level (7% on the 95% confidence level). Figure 15 shows the developments for the late season *SCD*.

Figure 15. Basin-based development of the late season *SCD*. The Theil–Sen slope is color coded and the corresponding *p*-values are hatched over it.

When considering the catchment areas, the trends for March are also reflected in the late season *SCD*. This applies to the catchment areas of the Baltic Sea. The largest decrease in the 95% confidence level shows the Danube with −0.95 days/year, followed by the Siberian North Coast with −0.54 days/year and the Kara Sea Coast with −0.52 days/year. Additionally, the fourth largest basin of this study—the river Yenisey—shows a significant decrease in *SCD* with −0.50 days/year. Positive trends occur again in basins in southern Canada, but they are not significant.

4. Discussion

The first research question was to answer whether the now 23-year data set of complete GSP data is sufficient to identify reliable trends. We are aware that the 30-year Climate Normal (*CN*) [53] determined by the WMO (the youngest completed is 1991–2020) were chosen in order to be able to make secured statements, and that our data set is of course smaller. Nevertheless, we want to put our results in this context. The global trend analysis of mountain areas of the *SCD* examined by [22] covered 38 years (1982–2020). A mean trend of −0.4 days/year was observed for this period, which agrees well with our pixel-based trend for the whole *SCD* of −0.44 days/year. We also succeeded in confirming the snow cover changes in Europe predicted by [54] based on regional climate models. As in their simulations, the Baltic Sea region turns out to be a hotspot for changing *SCD*, they see an *SCD* decrease of −0.55 days/year over 60 years for the *CN* 2071–2100 compared to *CN* 1961–1990. We found the largest significant decreases for the basin areas in the boreal spring and March. The Poland coast showed a similar decrease for this period of −0.47 days/year, while the Neman river was almost twice as much at −0.85 days/year. The *SCD* increase in northern Fennoscandia in the boreal spring shown in Figure 9 confirms

previous studies [26]. For the continental areas in Canada, the *SCD* increase found by [27] in the boreal spring (Figure 9) could be confirmed. However, e.g., the Nelson River showed a significant *SCD* increase of +0.31 days/year even in November, where [27] found a general decrease. In the month of November, the continental basins of Syr Darya and Lake Balkash in Asia also stood out with significant *SCD* increases (Figure 14). For Syr Darya, we found +0.27 days/year, which corresponds to the findings of the 28-year time series from [45]. The Lake Balkash catchment *SCD* increase of +0.29 days/year coincides with a climate change induced precipitation increase in this region of +0.654 mm/year [55]. The general *SCD* increase in Northeast China (NEC) in the Manchurian region also has climatological causes (see Figures 8–10). This is attributed by [56] (who studied the period 1985–2010) to a weakening of the East Asian Winter Monsoon (EAWM), which allows colder air to penetrate from the north. Along with increased water vapor content, this leads to increased snowfall in NEC. The comparisons with previous, mostly regional studies over longer periods of time show that our results of the 23 examined years confirmed previous findings but also new trends could be identified; 23 years are therefore sufficiently well suited to depicting trends.

The next point to discuss is the accuracy, on the one hand of the MODIS data itself, on the other hand of the gap-filled product. The absolute accuracy of this product is given by [57] as >93% depending on the land cover. The accuracy of MODIS on Aqua is slightly lower due to the defective band 6. In order to reliably determine trends, a correction for the gaps due to cloud cover is essential, since in Europe, for example, these cover 46.86% of the pixels for Terra and 48.47% for Aqua [43]. In the first step, the daily combination of Terra and Aqua, the accuracy remains at 92% [58,59]. The 3-day interpolation leads to hardly any deterioration in accuracy, and that of the topographical interpolation is given by [60] with 95%. Filling the remaining gaps with the pixel values of preceding days has a greater influence on the accuracy. The accuracy drops with increasing time steps, a cloud-persistence count (*CPC*) layer is included in our and the CGF product [61]. The filling of cloud gaps occurs mainly in the first few days with an exponential decrease. In the example from [61], 90% of the gaps were filled after just 5 days. After 10 days, there are usually no more gaps. A study by [3] in Chile was therefore satisfied with a temporal filling of up to 3 days and obtained almost cloud-free snow coverage. During the polar night, the gaps are of course larger, but due to the usually continuous snow cover during this time, there is no loss of accuracy either. The gap-free *SCD* is validated either indirectly with weighted individual accuracies of the different steps [58,62], or directly with measuring stations on the ground. The latter are unfortunately very unequally distributed or are missing entirely. In comparison with station data, [59] achieved an accuracy of 92.79–93.34% for the gap-free *SCD* data set in China; for the described GSP product, an accuracy of 86.66% was achieved for Europe (station data mainly exist in the Netherlands and Norway) [43]. For Chile the overall accuracy was between 81 and 92% [63]. For our global approach, np analysis of the accuracy was carried out so far, and due to the examined areas, only indirect validation is possible. An estimation of the accuracy based on the *CPC* is still in progress.

The next point is to discuss whether the chosen approach, which combines the MK test and Theil–Sen slope, is suitable. The combination of these has often been used for snow surface dynamics [17,64,65], but it also means that some developments remain undetected. Larger interannual *SCD* variations and fluctuations lead to a lower significance and are therefore not noticeable in such a large data set. On a regional scale, however, these strong fluctuations can already have catastrophic hydrological effects such as floods or droughts, as has been shown in [26]. The strength, or even the weakness, of the Theil–Sen slope calculation lies in the fact that such extremes are filtered out—even if these are not real outliers, but only reflect the natural variability. Alternatively, it would be advisable to rather use the coefficient of variance (*CV*; the standard deviation divided by the mean) [66]. This would also allow to better assess the significance of *SCD* changes, since, for example, one day less *SCD* per year has a smaller impact in the Arctic than in the central European low mountain ranges. There is also the question of whether the choice of catchment areas

as aggregation makes sense. From a hydrological point of view, this has definitely proven to be the case [28,29], but the set threshold values meant that only one basin in the southern hemisphere was examined. For the southern hemisphere, an investigation of mountainous areas as in [22] would therefore make more sense, since there is no extensive snow cover in the lowlands—but most of the seasonal snow cover occurs in the lowlands of the northern hemisphere [67]. This leads to the desired follow-up investigations, which are to be carried out with the data set (and the additional years).

In the future, evaluations should therefore be carried out according to altitude as well as meridional and zonal classification. Of course, this is then no longer globally feasible, but is applied to selected catchment areas that were shown in this study. The relatively snow-poor areas of the southern hemisphere should be considered by examining the global mountain ranges in a further study in order to be able to compare the results of the GSP processor directly with the work of [22]. Together with information on flora (*NDVI* and land cover classes), the influence of snow development on vegetation development is to be examined with regard to the important topic of greening of the Arctic [68].

5. Conclusions

In summary, it was found that the 23 years that are now available are already sufficient to determine significant trends for a considerable part of the observed areas. This was possible for the snow cover duration of the entire hydrological year in the 80% confidence interval for almost 25% of the observed area (pixel-based). For the sometimes very large (an aggregated) major basin areas of the FAO data set, it was shown that these are very well suited to interpreting the snow cover development averaged over the entire catchment area. Nevertheless, of course this study cannot replace detailed hydrological modeling (with additional area properties and meteorological conditions), and a closer look should certainly at least consider the relief dependency. However, we are showing an easy-to-implement possibility to achieve a global overview of basin-dependent *SCD* developments—and then to take a closer look at interesting basins. For both the pixel-based and basin-based analysis, we found a global general decrease in *SCD*. In some areas, there was also a shift in the snow cover season (earlier onset or delayed melt) with roughly the same overall duration.

Appendix A

The Mann–Kendall (MK) test [49,50] is used to determine whether there is a monotonic trend in a time series, and the Theil–Sen slope [51] is used to determine the magnitude of the trend. In the MK test, the null hypothesis (H_0) indicates no trend, while the alternative hypothesis indicates the presence of a trend. In the following, i and j stand for two consecutive years (where j is later than i), x_i and x_j stand for the *SCD* of the corresponding years. First, the strength of the sequence for the time series $X = (x_i, x_j, \ldots, x_n)$ is described by the MK statistic S is derived from Equations (A1) to (A2) [48]:

$$S = \sum_{i=1}^{n-1} \sum_{j=i+1}^{n} sgn(x_j - x_i) \tag{A1}$$

$$sgn(x_j - x_i) = \begin{cases} +1 \ (x_j - x_i > 0) \\ 0 \ (x_j - x_i = 0) \\ -1 \ (x_j - x_i < 0) \end{cases} \tag{A2}$$

After that, the variance of S depending on the number of years n is calculated using Equation (A3):

$$Var(S) = \frac{n(n-1)(2n+5)}{18} \tag{A3}$$

Finally, the Z statistic is calculated from S and $Var(S)$, which states whether there is a positive or negative trend (Equation (A4)):

$$Z = \begin{cases} \frac{S-1}{\sqrt{Var(S)}} \ (S > 0) \\ 0 \ (S = 0) \\ \frac{S+1}{\sqrt{Var(S)}} \ (S < 0) \end{cases} \tag{A4}$$

The trend is significant when $|Z| \geq Z_{(1-\alpha/2)}$, where α is the significance level corresponding to the *p*-value and can be set to e.g., 0.05. Finally, the magnitude of the trend (β) is calculated by the Theil–Sen slope (Equation (A5)):

$$\beta = Median\left(\frac{x_j - x_i}{j - i}\right) \tag{A5}$$

Appendix B

Since, for the sake of clarity, only the most relevant time periods are presented in the manuscript, the histograms for the pixel- and basin-based analysis are shown below. Figure A1 shows the histograms of the pixel-based analysis, Figure A2 shows the histograms of the basin-based analysis. In addition, Tables A1 and A2 show the mean slope values for the time periods and confidence intervals.

Table A1. Arithmetic mean of the slopes (scaled to days per year) of the pixel-based trend analysis for the three confidence intervals. Note that the pixels are a percentage of the total (not the total number N).

Period	CI 80% [Days/Year] (%)	CI 90% [Days/Year] (%)	CI 95% [Days/Year] (%)
01	−0.12 (13%)	−0.18 (6%)	−0.23 (3%)
02	−0.09 (11%)	−0.12 (5%)	−0.14 (2%)
03	−0.16 (12%)	−0.22 (6%)	−0.27 (3%)
04	−0.10 (11%)	−0.17 (5%)	−0.22 (2%)
05	−0.05 (13%)	−0.07 (6%)	−0.07 (3%)
06	−0.09 (11%)	−0.16 (5%)	−0.24 (3%)
07	−0.01 (12%)	−0.01 (4%)	−0.01 (2%)
08	0.00 (11%)	0.00 (4%)	−0.00 (2%)

Table A1. *Cont.*

Period	CI 80% [Days/Year] (%)	CI 90% [Days/Year] (%)	CI 95% [Days/Year] (%)
09	−0.02 (13%)	−0.04 (5%)	−0.05 (2%)
10	−0.07 (14%)	−0.11 (6%)	−0.14 (3%)
11	0.03 (14%)	0.04 (6%)	0.03 (3%)
12	−0.12 (13%)	−0.17 (6%)	−0.22 (3%)
SON	−0.04 (17%)	−0.07 (8%)	−0.11 (4%)
DJF	−0.29 (15%)	−0.40 (7%)	−0.48 (4%)
MAM	−0.20 (18%)	−0.28 (9%)	−0.35 (4%)
JJA	−0.07 (16%)	−0.12 (7%)	−0.17 (4%)
early	−0.14 (19%)	−0.18 (9%)	−0.22 (4%)
late	−0.33 (21%)	−0.43 (11%)	−0.52 (6%)
full	−0.44 (24%)	−0.57 (13%)	−0.69 (7%)

Figure A1. Histograms of derived Theil–Sen slopes of the pixel-based trend analysis of *SCD* for the 19 observed periods. The color coding represents the confidence intervals, and a normalization with the largest value was carried out.
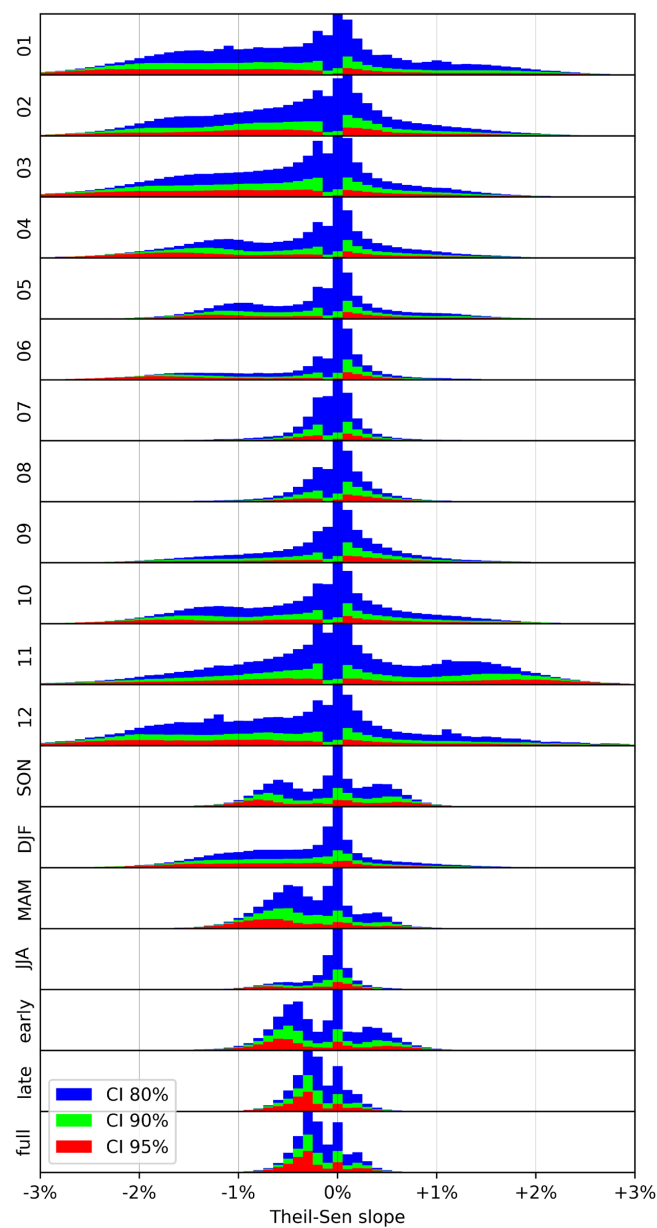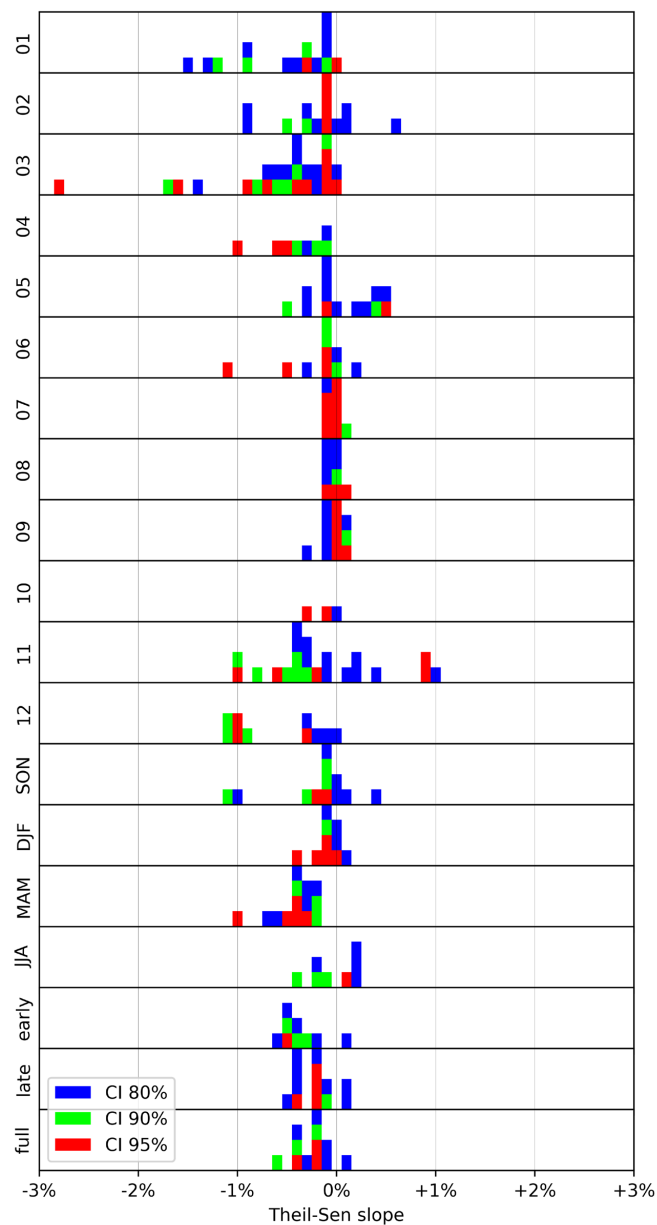
Figure A2. Histograms of derived Theil–Sen slopes of the basin-based trend analysis of *SCD* for the 19 observed periods. The color coding represents the confidence intervals, and a normalization with the largest value was carried out.

Table A2. Arithmetic mean of the slopes (scaled to days per year) of the basin-based trend analysis for the three confidence intervals. N shows the total number of basin areas.

Period	CI 80% [Days/Year] (N)	CI 90% [Days/Year] (N)	CI 95% [Days/Year] (N)
01	−0.15 (15)	−0.13 (6)	−0.03 (2)
02	−0.03 (19)	−0.04 (6)	−0.01 (4)
03	−0.16 (28)	−0.20 (16)	−0.20 (10)
04	−0.10 (8)	−0.12 (6)	−0.19 (3)
05	0.03 (15)	0.04 (4)	0.08 (2)
06	−0.03 (16)	−0.06 (7)	−0.11 (4)
07	0.00 (18)	0.01 (10)	0.00 (9)
08	0.00 (9)	0.01 (4)	0.01 (3)
09	0.00 (14)	0.02 (7)	0.01 (6)
10	−0.03 (3)	−0.04 (2)	−0.04 (2)

Table A2. *Cont.*

Period	CI 80% [Days/Year] (N)	CI 90% [Days/Year] (N)	CI 95% [Days/Year] (N)
11	−0.03 (23)	−0.08 (11)	0.01 (5)
12	−0.17 (10)	−0.26 (6)	−0.22 (3)
SON	−0.13 (14)	−0.23 (6)	−0.06 (2)
DJF	−0.03 (11)	−0.09 (6)	−0.10 (5)
MAM	−0.33 (14)	−0.33 (8)	−0.42 (5)
JJA	0.02 (8)	−0.10 (4)	0.13 (1)
early	−0.42 (9)	−0.51 (4)	−0.55 (1)
late	−0.42 (15)	−0.42 (5)	−0.48 (4)
full	−0.72 (12)	−1.02 (6)	−0.77 (3)

References

1. Hall, D.K.; Riggs, G.A.; Salomonson, V.V. Development of methods for mapping global snow cover using moderate resolution imaging spectroradiometer data. *Remote Sens. Environ.* **1995**, *54*, 127–140. [CrossRef]
2. Pepe, M.; Brivio, P.A.; Rampini, A.; Nodari, F.R.; Boschetti, M. Snow cover monitoring in alpine regions using ENVISAT optical data. *Int. J. Remote Sens.* **2005**, *26*, 4661–4667. [CrossRef]
3. Goodrich, L.E. The influence of snow cover on the ground thermal regime. *Can. Geotech. J.* **1982**, *19*, 421–432. [CrossRef]
4. GCOS, WMO. *Systematic Observation Requirements for Satellite-Based Data Products for Climate—2011 Update*; GCOS, WMO: Geneva, Switzerland, 2011.
5. Mankin, J.S.; Viviroli, D.; Singh, D.; Hoekstra, A.Y.; Diffenbaugh, N.S. The potential for snow to supply human water demand in the present and future. *Environ. Res. Lett.* **2015**, *10*, 114016. [CrossRef]
6. Winkler, D.E.; Butz, R.J.; Germino, M.J.; Reinhardt, K.; Kueppers, L.M. Snowmelt timing regulates community composition, phenology, and physiological performance of alpine plants. *Front. Plant Sci.* **2018**, *9*, 1140. [CrossRef]
7. Elder, K.; Dozier, J.; Michaelsen, J. Snow accumulation and distribution in an alpine watershed. *Water Resour. Res.* **1991**, *27*, 1541–1552. [CrossRef]
8. Dietz, A.J.; Kuenzer, C.; Gessner, U.; Dech, S. Remote sensing of snow—A review of available methods. *Int. J. Remote Sens.* **2012**, *33*, 4094–4134. [CrossRef]
9. Painter, T.H.; Berisford, D.F.; Boardman, J.W.; Bormann, K.J.; Deems, J.S.; Gehrke, F.; Hedrick, A.; Joyce, M.; Laidlaw, R.; Marks, D.; et al. The airborne snow observatory: Fusion of scanning lidar, imaging spectrometer, and physically-based modeling for mapping snow water equivalent and snow albedo. *Remote Sens. Environ.* **2016**, *184*, 139–152. [CrossRef]
10. Chang, A.T.C.; Foster, J.L.; Hall, D.K.; Robinson, D.A.; Peiji, L.; Meisheng, C. The use of microwave radiometer data for characterizing snow storage in Western China. *Ann. Glaciol.* **1992**, *16*, 215–219. [CrossRef]
11. Kelly, R.E.; Chang, A.T.; Tsang, L.; Foster, J.L. A prototype AMSR-e global snow area and snow depth algorithm. *IEEE Trans. Geosci. Remote Sens.* **2003**, *41*, 230–242. [CrossRef]
12. Tsai, Y.L.S.; Dietz, A.; Oppelt, N.; Kuenzer, C. Wet and dry snow detection using Sentinel-1 SAR data for mountainous areas with a machine learning technique. *Remote Sens.* **2019**, *11*, 895. [CrossRef]
13. Koehler, J.; Bauer, A.; Dietz, A.J.; Kuenzer, C. Towards forecasting future snow cover dynamics in the European Alps—The potential of long optical remote-sensing time series. *Remote Sens.* **2022**, *14*, 4461. [CrossRef]
14. Hall, D.K.; Riggs, G.A.; Salomonson, V.V.; DiGirolamo, N.E.; Bayr, K.J. MODIS snow-cover products. *Remote Sens. Environ.* **2002**, *83*, 181–194. [CrossRef]
15. Ackroyd, C.; Skiles, S.M.; Rittger, K.; Meyer, J. Trends in snow cover duration across river basins in high mountain asia from daily Gap-Filled MODIS fractional snow covered area. *Front. Earth Sci.* **2021**, *9*, 713145. [CrossRef]
16. Malmros, J.K.; Mernild, S.H.; Wilson, R.; Tagesson, T.; Fensholt, R. Snow cover and snow Albedo changes in the central andes of Chile and Argentina from Daily MODIS Observations (2000–2016). *Remote Sens. Environ.* **2018**, *209*, 240–252. [CrossRef]
17. Saavedra, F.A.; Kampf, S.K.; Fassnacht, S.R.; Sibold, J.S. Changes in andes snow cover from MODIS data, 2000–2016. *Cryosphere* **2018**, *12*, 1027–1046. [CrossRef]
18. Xiao, L.; Che, T.; Chen, L.; Xie, H.; Dai, L. Quantifying snow albedo radiative forcing and its feedback during 2003–2016. *Remote Sens.* **2017**, *9*, 883. [CrossRef]
19. Zhou, H.; Aizen, E.; Aizen, V. Deriving long term snow cover extent dataset from AVHRR and MODIS data: Central Asia case study. *Remote Sens. Environ.* **2013**, *136*, 146–162. [CrossRef]
20. Premier, V.; Marin, C.; Steger, S.; Notarnicola, C.; Bruzzone, L. A novel approach based on a hierarchical multiresolution analysis of optical time series to reconstruct the daily high-resolution snow cover area. *IEEE J. Sel. Top. Appl. Earth Obs. Remote Sens.* **2021**, *14*, 9223–9240. [CrossRef]
21. Revuelto, J.; Alonso-González, E.; Gascoin, S.; Rodríguez-López, G.; López-Moreno, J.I. Spatial downscaling of MODIS snow cover observations using Sentinel-2 snow products. *Remote Sens.* **2021**, *13*, 4513. [CrossRef]
22. Notarnicola, C. Overall negative trends for snow cover extent and duration in global mountain regions over 1982–2020. *Sci Rep* **2022**, *12*, 13731. [CrossRef] [PubMed]

23. Hall, D.K.; Riggs, G.A.; Foster, J.L.; Kumar, S.V. Development and evaluation of a cloud-gap-filled MODIS daily snow-cover product. *Remote Sens. Environ.* **2010**, *114*, 496–503. [CrossRef]

24. Dietz, A.J.; Kuenzer, C.; Dech, S. Global SnowPack: A new set of snow cover parameters for studying status and dynamics of the planetary snow cover extent. *Remote Sens. Lett.* **2015**, *6*, 844–853. [CrossRef]

25. Dunn, R.J.H.; Aldred, F.; Gobron, N.; Miller, J.B.; Willett, K.M.; Ades, M.; Adler, R.; Allan, R.P.; Allan, R. Global climate. *Bull. Am. Meteorol. Soc.* **2021**, *102*, S11–S142. [CrossRef]

26. Rößler, S.; Witt, M.S.; Ikonen, J.; Brown, I.A.; Dietz, A.J. Remote sensing of snow cover variability and its influence on the Runoff of Sápmi's Rivers. *Geosciences* **2021**, *11*, 130. [CrossRef]

27. Brown, R.D.; Smith, C.; Derksen, C.; Mudryk, L. Canadian in situ snow cover trends for 1955–2017 including an assessment of the impact of automation. *Atmos. Ocean* **2021**, *59*, 77–92. [CrossRef]

28. Atif, I.; Iqbal, J.; Mahboob, M. Investigating snow cover and hydrometeorological trends in contrasting hydrological regimes of the Upper Indus Basin. *Atmosphere* **2018**, *9*, 162. [CrossRef]

29. Blahušiaková, A.; Matoušková, M.; Jenicek, M.; Ledvinka, O.; Kliment, Z.; Podolinská, J.; Snopková, Z. Snow and climate trends and their impact on seasonal runoff and hydrological drought types in selected mountain catchments in Central Europe. *Hydrol. Sci. J.* **2020**, *65*, 2083–2096. [CrossRef]

30. Desinayak, N.; Prasad, A.K.; El-Askary, H.; Kafatos, M.; Asrar, G.R. Snow cover variability and trend over the Hindu Kush Himalayan Region using MODIS and SRTM data. *Ann. Geophys.* **2022**, *40*, 67–82. [CrossRef]

31. Niu, G.-Y.; Yang, Z.-L. An observation-based formulation of snow cover fraction and its evaluation over large north american river basins. *J. Geophys. Res.* **2007**, *112*, D21101. [CrossRef]

32. Hoogeveen, J.; Faurès, J.-M.; Peiser, L.; Burke, J.; van de Giesen, N. GlobWat—A Global Water Balance Model to Assess Water Use in Irrigated Agriculture. *Hydrol. Earth Syst. Sci.* **2015**, *19*, 3829–3844. [CrossRef]

33. Wang, L.; Lv, A. Identification and diagnosis of transboundary river basin water management in china and neighboring countries. *Sustainability* **2022**, *14*, 12360. [CrossRef]

34. Hall, D.K.; Riggs, G.A. Normalized-Difference Snow Index (NDSI). In *Encyclopedia of Snow, Ice and Glaciers*; Singh, V.P., Singh, P., Haritashya, U.K., Eds.; Encyclopedia of Earth Sciences Series; Springer: Dordrecht, The Netherlands, 2011; pp. 779–780. ISBN 978-90-481-2641-5.

35. Hall, D.K.; Riggs, G.A. *MODIS/Terra Snow Cover 5-Min L2 Swath 500m*, Version 61; National Snow and Ice Data Center: Boulder, CO, USA, 2021; Digital media.

36. Hall, D.K.; Riggs, G.A. *MODIS/Aqua Snow Cover 5-Min L2 Swath 500m*, Version 61; National Snow and Ice Data Center: Boulder, CO, USA, 2021; Digital media.

37. Snyder, J.P. Map Projections–a Working Manual. Washington, DC: United States Government Printing Office. *US Geol. Surv. Prof. Pap.* **1987**, *1395*, 96.

38. Riggs, G.A.; Hall, D.K.; Salomonson, V.V. A snow index for the landsat thematic mapper and moderate resolution imaging spectroradiometer. In Proceedings of the IGARSS '94—1994 IEEE International Geoscience and Remote Sensing Symposium, Pasadena, CA, USA, 8–12 August 1994; IEEE: Pasadena, CA, USA, 1994; Volume 4, pp. 1942–1944.

39. Salomonson, V.V.; Appel, I. Estimating fractional snow cover from MODIS using the normalized difference snow index. *Remote Sens. Environ.* **2004**, *89*, 351–360. [CrossRef]

40. Klein, A.G.; Hall, D.K.; Riggs, G.A. Improving snow cover mapping in forests through the use of a canopy reflectance model. *Hydrol. Process.* **1998**, *12*, 1723–1744. [CrossRef]

41. Li, X.; Jing, Y.; Shen, H.; Zhang, L. The recent developments in cloud removal approaches of MODIS snow cover product. *Hydrol. Earth Syst. Sci.* **2019**, *23*, 2401–2416. [CrossRef]

42. Fugazza, D.; Manara, V.; Senese, A.; Diolaiuti, G.; Maugeri, M. Snow cover variability in the greater alpine region in the MODIS era (2000–2019). *Remote Sens.* **2021**, *13*, 2945. [CrossRef]

43. Dietz, A.J.; Wohner, C.; Kuenzer, C. European snow cover characteristics between 2000 and 2011 derived from improved MODIS daily snow cover products. *Remote Sens.* **2012**, *4*, 2432–2454. [CrossRef]

44. Wang, X.; Xie, H. New methods for studying the spatiotemporal variation of snow cover based on combination products of MODIS terra and aqua. *J. Hydrol.* **2009**, *371*, 192–200. [CrossRef]

45. Dietz, A.; Conrad, C.; Kuenzer, C.; Gesell, G.; Dech, S. Identifying changing snow cover characteristics in Central Asia between 1986 and 2014 from remote sensing data. *Remote Sens.* **2014**, *6*, 12752–12775. [CrossRef]

46. Food and Agriculture Organization of the United Nations, FAO Land and Water Division. Major Hydrological Basins of the World. Available online: https://data.apps.fao.org/catalog//iso/7707086d-af3c-41cc-8aa5-323d8609b2d1 (accessed on 17 August 2022).

47. Riggs, G.; Hall, D. Continuity of MODIS and VIIRS snow cover extent data products for development of an earth science data record. *Remote Sens.* **2020**, *12*, 3781. [CrossRef]

48. Zou, Y.; Sun, P.; Ma, Z.; Lv, Y.; Zhang, Q. Snow cover in the three stable snow cover areas of china and spatio-temporal patterns of the future. *Remote Sens.* **2022**, *14*, 3098. [CrossRef]

49. Mann, H.B. Nonparametric tests against trend. *Econometrica* **1945**, *13*, 245. [CrossRef]

50. Kendall, M.G. *Rank Correlation Methods*; Charles Griffin Book Series; Oxford University Press: London, UK, 1975.

51. Sen, P.K. Estimates of the regression coefficient based on Kendall's Tau. *J. Am. Stat. Assoc.* **1968**, *63*, 1379–1389. [CrossRef]

52. Hussain, M.; Mahmud, I. PyMannKendall: A python package for non parametric Mann Kendall family of trend tests. *JOSS* **2019**, *4*, 1556. [CrossRef]

53. Arguez, A.; Durre, I.; Applequist, S.; Vose, R.S.; Squires, M.F.; Yin, X.; Heim, R.R.; Owen, T.W. NOAA's 1981–2010 U.S. Climate normals: An overview. *Bull. Am. Meteorol. Soc.* **2012**, *93*, 1687–1697. [CrossRef]

54. Jylhä, K.; Fronzek, S.; Tuomenvirta, H.; Carter, T.R.; Ruosteenoja, K. Changes in frost, snow and baltic sea ice by the end of the twenty-first century based on climate model projections for Europe. *Clim. Chang.* **2008**, *86*, 441–462. [CrossRef]

55. Guo, L.; Xia, Z. Temperature and precipitation long-term trends and variations in the Ili-Balkhash Basin. *Theor. Appl Clim.* **2014**, *115*, 219–229. [CrossRef]

56. Wang, H.; He, S. The increase of snowfall in Northeast China after the Mid-1980s. *Chin. Sci. Bull.* **2013**, *58*, 1350–1354. [CrossRef]

57. Hall, D.K.; Riggs, G.A. Accuracy assessment of the MODIS snow products. *Hydrol. Process.* **2007**, *21*, 1534–1547. [CrossRef]

58. Dietz, A.J.; Kuenzer, C.; Conrad, C. Snow-cover variability in Central Asia between 2000 and 2011 derived from improved MODIS daily snow-cover products. *Int. J. Remote Sens.* **2013**, *34*, 3879–3902. [CrossRef]

59. Liu, J.; Zhang, W.; Liu, T. Monitoring recent changes in snow cover in Central Asia using improved MODIS snow-cover products. *J. Arid Land* **2017**, *9*, 763–777. [CrossRef]

60. Parajka, J.; Pepe, M.; Rampini, A.; Rossi, S.; Blöschl, G. A regional snow-line method for estimating snow cover from MODIS during cloud cover. *J. Hydrol.* **2010**, *381*, 203–212. [CrossRef]

61. Hall, D.K.; Riggs, G.A.; DiGirolamo, N.E.; Román, M.O. Evaluation of MODIS and VIIRS cloud-gap-filled snow-cover products for production of an earth science data record. *Hydrol. Earth Syst. Sci.* **2019**, *23*, 5227–5241. [CrossRef]

62. Gafurov, A.; Bárdossy, A. Cloud removal methodology from MODIS snow cover product. *Hydrol. Earth Syst. Sci.* **2009**, *13*, 1361–1373. [CrossRef]

63. Mattar, C.; Fuster, R.; Perez, T. Application of a cloud removal algorithm for snow-covered areas from daily MODIS imagery over Andes Mountains. *Atmosphere* **2022**, *13*, 392. [CrossRef]

64. Choudhury, A.; Yadav, A.C.; Bonafoni, S. A Response of snow cover to the climate in the Northwest Himalaya (NWH) using satellite products. *Remote Sens.* **2021**, *13*, 655. [CrossRef]

65. Thapa, A.; Muhammad, S. Contemporary snow changes in the Karakoram Region attributed to improved MODIS data between 2003 and 2018. *Water* **2020**, *12*, 2681. [CrossRef]

66. Helbig, N.; van Herwijnen, A.; Magnusson, J.; Jonas, T. Fractional snow-covered area parameterization over complex topography. *Hydrol. Earth Syst. Sci.* **2015**, *19*, 1339–1351. [CrossRef]

67. Lemke, P.; Ren, J.; Alley, R.B.; Allison, I.; Carrasco, J.; Flato, G.; Fujii, Y.; Kaser, G.; Mote, P.; Thomas, R.H.; et al. Observations: Changes in snow, ice and frozen ground. In *Climate Change 2007: The Physical Science Basis*; Contribution of Working Group I to the Fourth Assessment Report of the Intergovernmental Panel on Climate Change; Solomon, S., Qin, D., Manning, M., Chen, Z., Marquis, M., Averyt, K.B., Tignor, M., Miller, H.L., Eds.; Cambridge University Press: Cambridge, UK; New York, NY, USA, 2007.

68. Swanson, D. Trends in greenness and snow cover in Alaska's Arctic national parks, 2000–2016. *Remote Sens.* **2017**, *9*, 514. [CrossRef]